Investigation of Fabry Perot Interferometer Temperature Sensor Based on Hollow Core Anti-Resonance Optical Fiber

Qiming Wang, Bin Li [ID], Rongxu Shen, Xin Yan [ID], Xuenan Zhang [ID], Fang Wang [ID], Takenobu Suzuki [ID], Yasutak Ohishi [ID], *Member, IEEE*, and Tonglei Cheng [ID]

Abstract—A Fabry-Perot interferometer (FPI) temperature sensor was proposed by splicing a self-made hollow core anti-resonance fiber (HC-ARF) between two single mode fibers (SMFs). The HC-ARF was 2 mm long and one SMF was 20 mm in length. The SMF end face was coated with an Au film. When temperature varied from 45 °C to 85 °C, a sensitivity of 81.1 pm/°C was obtained at the waveband of 1550 nm∼1555 nm. When temperature varied from 35 °C to 95 °C, a sensitivity of 138.8 pm/°C was obtained at the waveband of 1571 nm∼1581 nm. Theoretical analysis suggested that the sensitivity of this proposed sensor can be easily adjusted by varying the length of the Au-coated SMF via the Vernier effect, which was confirmed by a subsequent experiment where the SMF length was varied from 20 mm to 170 mm. This work offers a simple sensitivity control method, and the proposed sensor is easy to manufacture, compact in structure, and convenient in performance control, which can be applied for a wide range of biological and chemical applications.

Index Terms—Hollow Core anti-resonance fiber (HC-ARFs), Fabry Perot Interferometer (FPI), temperature sensor.

I. Introduction

AN ACCURATE and real-time measurement of temperature is essentially important for process control in fields of food processing and health, agricultural biological manufacturing and electronic manufacturing, etc. Demonstrating advantages of strong anti-interference, compact structure, easy layout and online monitoring [4], [5], optical fiber temperature sensors have been widely used in various industries and environments, for instance, petroleum exploration, marine monitoring, biomedical [1] and aerospace engineering [2], [3], etc. With the development of optical fiber sensing technology, more recently, a variety of novel temperature sensors have been developed based on Bragg fiber [6], [7], stress-optical effect (SOE) [8], Michelson interferometer (MI)[9], Mach-Zehnder interferometer (MZI) [10], hollow fiber interferometer (HI) [11], [12] and Fabry-Perot interferometer (FPI) [13], [14]. Although these optical fiber temperature sensors have been well exploited and widely applied, they still have problems such as high manufacturing difficulty [13], [14], rigid machining accuracy or special splicing. Particularly, their sensitivity needs to be improved [5]–[13].

The optical Vernier effect, which was proposed by Urquhart in 1988 [15] and which happens when the FSRs of the FP cavities are close [16], has been acknowledged to be an effective and simple way to improve the temperature sensing sensitivity. Based on this effect, Mingran Quan *et al.* obtained a RI sensitivity of 30899 nm/RIU in 2015 [17], Chen Zhu and Jie Huang obtained a sensitivity of −10.58 kHz/°C using a two-cascaded-FPIs-OCMI in 2021 [18]. Recently, Marta S. Ferreira *et al.* proposed a sensor with a temperature sensitivity of 41.7 pm/°C and a strain sensitivity of 2.5 pm/$\mu\varepsilon$ by exploiting the Vernier effect of a specially spliced hollow core anti-resonance fiber (HC-ARF). The HC-ARF has the advantage of low loss, large bandwidth and exceptional polarization purity [21]–[23]. Moreover, its light guiding mechanism follows the anti-resonant reflecting optical waveguide (ARROW) effect which is highly sensitive to the environmental RI change, and the multiple mode interference (MMI) can also contribute to improving the sensor's performance [24], [25]. Although the HC-ARF has proved its application values in the sensing field [19], [24]–[30], its fabrication sometimes needs special splicing which is hard to control.

In this paper, a FPI temperature sensor was designed and experimentally investigated based on a self-made HC-ARF, where a sensitivity of 138.8 pm/°C and 81.1 pm/°C was respectively realized at the waveband of 1571 nm∼1581 nm and 1550 nm∼1555 nm when temperature respectively varied

Qiming Wang, Bin Li, Rongxu Shen, Xin Yan, Xuenan Zhang, and Fang Wang are with the State Key Laboratory of Synthetical Automation for Process Industries, College of Information Science and Engineering, Northeastern University, Shenyang 110819, China (e-mail: 1810319@stu.neu.edu.cn; li5605220@163.com; 1406798424@qq.com; yanxin@ise.neu.edu.cn; zhangxuenan@ise.neu.edu.cn; wangfang@ise.neu.edu.cn).

Takenobu Suzuki and Yasutak Ohishi are with the Research Center for Advanced Photon Technology, Toyota Technological Institute, Nagoya 468-8511, Japan (e-mail: takenobu@toyota-ti.ac.jp; ohishi@toyota-ti.ac.jp).

Tonglei Cheng is with the State Key Laboratory of Synthetical Automation for Process Industries, College of Information Science and Engineering, Northeastern University, Shenyang 110819, China, and also with the Hebei Key Laboratory of Micro-Nano Precision Optical Sensing and Measurement Technology, Qinhuangdao 066004, China (e-mail: chengtonglei@gmail.com).

Digital Object Identifier 10.1109/JPHOT.2021.3123977

Fig. 1. The fabrication process of HC-ARF (a) preform tube, (b) first drawing, (c) second drawing.

Fig. 2. (a) Microscopic picture of the cross-section of HC-ARF, (b) specific size data, (c) transmission spectrum from 600 nm to 2000 nm.

from 35 °C to 95 °C and from 45 °C to 85 °C. Theoretical and experimental investigation revealed that the sensitivity of the proposed sensor structure can be regulated by adjusting the length of the Au-coated SMF. The sensor design in this work offers a simple method to control sensitivity. Compared with other sensors reported previously [5]–[13], [19], the proposed sensor is easy to manufacture, compact in structure, convenient in performance control, and exhibits different sensitivities at different wavebands, which can be applied for a wide range of biological and chemical applications.

II. SENSOR PREPARATION

The HC-ARF used in this work was fabricated at our lab, the preparation process of which is shown by the following Fig. 1. First, nine silicon glass tubes with a diameter of 4 mm was used to form a preform tube with a diameter of 20 mm, as shown in Fig. 1(a). Then the preform was drawn into a glass tube of 3 mm in diameter using the graphite furnace at 1810 °C, as shown in Fig. 1(b). After that, the as-prepared glass tube was put into a glass sleeve with a diameter of 8 mm, and finally drawn into the HC-ARF of 150 um in diameter, as shown in Fig. 1(c). During the fabrication process, argon of 8kPa was used to keep the interstitial hole formation in the core-cladding interface.

The cross-section image of the fabricated HC-ARF has a nine-sided structure, as shown in Fig. 2(a). The external diameter of the fabricated HC-ARF was about 156 μm. The central core radius was 34 um, with a thickness of 0.8 um or 1.1 um, and the cladding wall was 36.6 um. The specific structure data has been marked in Fig. 2(b). The transmission spectrum measured using a Supercontinuum Light Source SC-5-FC is presented in
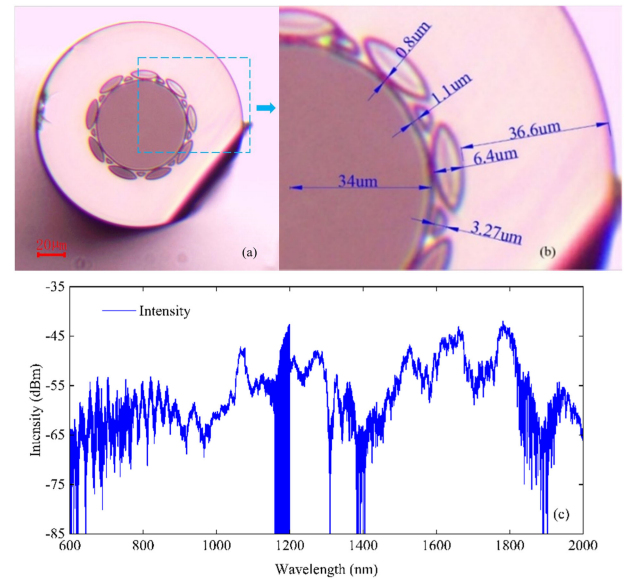
Fig. 2(c), which is obviously an anti-resonant fiber spectrum. The fiber loss varied greatly in the 1500~1600 nm and a high loss dip appeared near 1560 nm, which significantly affected part of the high order mode transmitted in different wavebands. It can lead to obviously different changes in the interference spectrum at different wavebands.

The proposed temperature sensor was made by splicing a section of HC-ARF (2 mm in length) between two sections of single mode fiber (SMF28) using a fusion splicer (FITEL S179C) switched to the manual mode. The arc discharge power was set to 60 arb units, the discharge time 500 ms (for comparison, an automatic splicing of two SMF28 has a discharge power of 100 arb units and a time of 2000 ms). The HC-ARF and the SMF were aligned axially and placed as close as possible but not in direct contact. To ensure the splicing stability and the internal fiber structure, the arc discharge was applied in the middle of the two fibers. Finally, an Au film was coated on the SMF vertical end face by plasma magnetron sputtering coating instrument (VTC-16-SM). For better cutting and splicing, the length of Au-coated SMF should not be less than 20 mm. Fig. 3 shows a successfully fabricated sensor with a 2 mm HC-ARF and a 20 mm Au-coated-SMF.

III. SENSING PRINCIPLES

Without the Au film, the proposed sensor structure can be regarded as a low-finesse FPI, which approximates a two-wave interferometer shown in Fig. 4 (without the blue dotted area). It only has two reflective surfaces: the first SMF/HC-ARF interface can be considered as Mirror M1 and the other interface as M2. The reflection coefficient of M1 is $R_1 = (n_{SMF} - n_{ARF})^2/(n_{SMF} + n_{ARF})^2$, where n_1 is the effective RI of the HC-ARF, n_{SMF} is the effective RI of the SMF [17], and α_1 is the transmission loss of the M1 surface. Correspondingly, the reflection coefficient of M2 is R_2, which is equal to R_1.
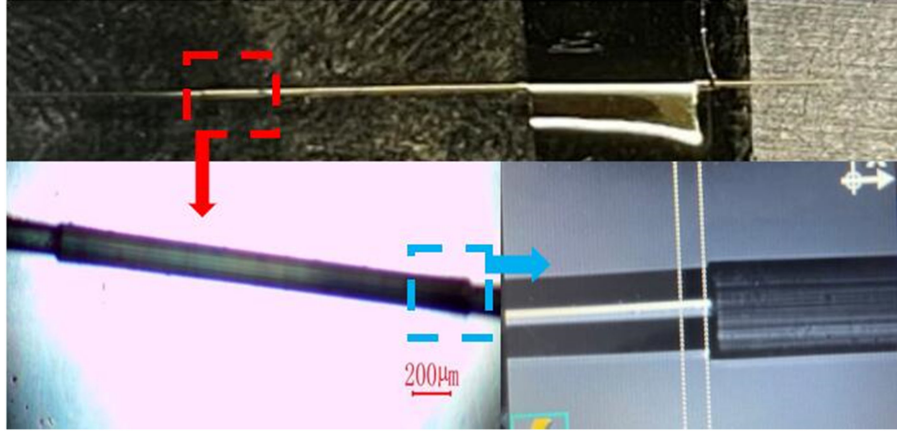
Fig. 3. The splicing details of a fabricated sensor with a 2 mm HC-ARF and a 20 mm-SMF2.
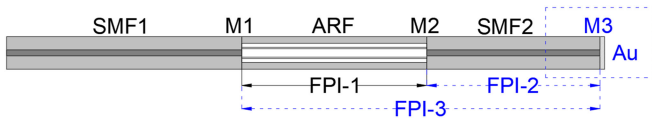

Fig. 4. Schematic design of the FPI sensor.

The light loss in the ARF cavity, including the effects due to mode mismatch and beam expansion, can be accounted for as the coefficient β_1. According to the electric field formula for a low-finesse FPI, the normalized reflection intensity I can be estimated as:

$$I = R_1 + A + 2\sqrt{AR_1} \cos \varphi_1 \tag{1}$$

$$A = (1 - \alpha_1)^2 (1 - \beta_1)^2 (1 - R_1)^2 R_2 \tag{2}$$

where $\varphi_1 = 4\pi n_{ARF} L_{ARF}/\lambda$ is propagation shift, L_{ARF} is the length of the HC-ARF and λ is the vacuum wavelength. From the above equations, we can see that I is theoretically independent of the SMF2 length (L_{SMF})

The spectrum generation of the proposed sensor structure without the Au film is under the combined effect of the thermal refractive index change of the fiber and the thermal expansion of the FP cavity [5]. The temperature sensitivity of the dense fringes can be obtained by [31], [32]

$$S_{ARF} = \frac{\partial \lambda}{\partial T} = \left(\frac{1}{n_{ARF}} \frac{\partial n_{ARF}}{\partial T} + \frac{1}{L_{ARF}} \frac{\partial L_{ARF}}{\partial T} \right) \lambda$$
$$= (\alpha_T + \xi_T) \lambda \tag{3}$$

where α_T is the thermo-optic coefficient and ξ_T is the thermal expansion coefficient. According to Equation (3), a real-time temperature measurement can be achieved by monitoring the wavelength shift of the reflection spectrum [31], [32]. Because the low-finesse FPI is theoretically insensitive to temperature, a mixed interference is introduced cladding an Au film to the HC-ARF structure.

With the addition of Au film, different interferometric paths are created, which generates three FPIs, as shown in Fig. 4 (include the blue dotted area). The input light coming from

the SMF1 core suffers a first reflection at Mirror M1, a second reflection at Mirror M2, and a third reflection at the SMF/Au interface, namely, M3. As a result, an FPI with a cavity length of L_{ARF} (FPI-1) and an FPI with a cavity length of L_{SMF} (FPI-2) are formed, together with another FPI (FPI-3) formed by M1 and M3. These three FPIs can be taken as a hybrid interferometer as a whole. The reflection intensity I can be expressed using the three-beam optical interference equation:

$$I = R_1 + A + B + 2\sqrt{R_1 B} \cos (\varphi_1 + \varphi_2)$$
$$+ 2\sqrt{R_1 A} \cos (\varphi_1) + 2\sqrt{AB} \cos (\varphi_2) \tag{4}$$

$$A = (1 - \alpha_1)^2 (1 - \beta_1)^2 (1 - R_1)^2 R_2 \tag{5}$$

$$B = (1 - \alpha_1)^2 (1 - \alpha_2)^2 (1 - \beta_1)^2$$
$$\times (1 - \beta_2)^2 (1 - R_2)^2 (1 - R_1)^2 R_3 \tag{6}$$

where R_3 is the reflection coefficient of M3 and $R_3 = (n_{SMF} - n_{Au})^2/(n_{SMF} + n_{Au})^2$, n_{Au} is the effective refractive index of Au film, $\varphi_2 = 4\pi n_{SMF} L_{SMF}/\lambda$ is propagation shift, and α_2 is the transmission loss of the M2 surface. Light loss of SMF2 can be accounted for as the coefficient β_2.

The FPI-1, FPI-2 and FPI-3 are designed to produce Vernier effect and an envelope will appear in the spectrum. The Vernier effect can significantly amplify waveform changes and thus improve the temperature sensitivity [14]–[16], [21]–[24]. The corresponding free spectral range (FSR) can be derived as [17], [19], [21]–[24]

$$FSR_1 \approx \frac{\lambda^2}{2n_{ARF} L_{ARF}} \tag{7}$$

$$FSR_2 \approx \frac{\lambda^2}{2n_{SMF} L_{SMF}} \tag{8}$$

$$FSR_3 \approx \frac{\lambda^2}{2 (n_{ARF} L_{ARF} + n_{SMF} L_{SMF})} \tag{9}$$

When the M3 reflection is weak, FPI-3 would be much weaker than FPI-2 and FPI-1, hardly causing any effect on the envelope. Under this situation, the FSR of the sensor (FSRS) can be derived
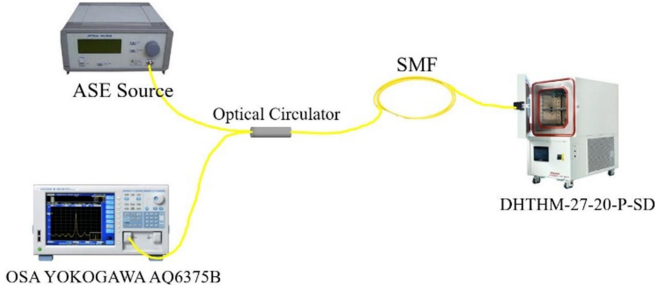
Fig. 5. Diagram of the experiment set up.

as [17], [19], [24]–[28]

$$FSR_S = \frac{FSR_2 \cdot FSR_1}{|FSR_1 - FSR_2|} \tag{10}$$

However, when the M3 reflection is strong, FPI-3 will affect the envelope, and FSRS can be derived as [17], [19], [24], [25], [33]–[36]

$$FSR_S = \frac{FSR_3 \cdot FSR_1}{|FSR_1 - kFSR_3|} \tag{11}$$

where k = [FSR1/FSR2].

The temperature sensitivity adjustment coefficient K and the temperature sensitivity S can be respectively expressed as [16], [19], [24], [25], [33]–[36]

$$K = \frac{FSR_1}{|FSR_1 - kFSR_3|} \tag{12}$$

$$S = S_{ARF} K \tag{13}$$

Based on Equation (6)–(8), when the length of SMF2 is changed, the temperature sensitivity adjustment coefficient (K') and the temperature sensitivity (S') of a similar waveband can be expressed as

$$K' = \frac{L_{SMF}}{L_{SMF}'} K \tag{14}$$

$$S' = \frac{L_{SMF}}{L_{SMF}'} S \tag{15}$$

where L_{SMF}' is the changed length of SMF2. We can see that the temperature sensitivity is directly related with the length change of SMF2, thus the sensor performance can be adjusted by varying the SMF2 length of the designed Au-coated sensor, which greatly simplify the sensors preparation and application convenience. In addition, the Au-coated film improves the sensitivity of the sensor at the same time, has oxidation resistance and a certain hardness, can play a protective role on the fiber end face, improve the damage resistance of the sensor.

IV. EXPERIMENTAL INVESTIGATION AND DISCUSSION

The experimental investigation concerning the temperature sensing performance of the proposed sensor was set up based on a typical reflection system, as presented in Fig. 5. A thermostat (DHTHM-27-20-P-SD) was responsible for the temperature adjustment. An ASE source with a bandwidth of
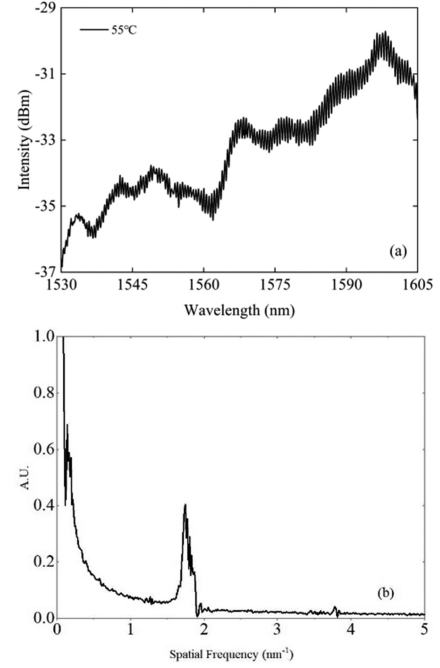

Fig. 6. (a) The FPI spectrum measured at 55 °C, (b) the corresponding FFT.

1520 nm∼1610 nm was adopted as the light source. The optical spectrum analyzer (OSA YOKOGAWA AQ6375B 1200-2400 nm) had a resolution of 0.05 nm and a sample interval of 0.01 nm. Temperature adjustment was realized by placing the sensor in a thermostat ((DHTHM-27-20-P-SD, with a resolution of 0.1 °C) which gradually heated from 35 °C to 95 °Cwith an interval of 10 °C. Each temperature change step was maintained for 10 min to assure the stability of the transmission spectrum.

As mentioned in Section II, the proposed HC-ARF sensor coated with an Au-coated film can be taken as a hybrid interferometer. Here the sensor was proposed to have a HC-ARF of 2 mm in length and an Au-coated SMF of 20 mm in length (the end of SMF2 experienced a sputter coating of 40s using VTC-16-SM). The FPI spectrum measured at 55 °C is shown in Fig. 6(a), and the result after going through the Fast Fourier Transform (FFT) is shown in Fig. 6(b). As expected, the FFT curve exhibited the typical behavior of a hybrid interferometer and generated two distinct frequencies.

The spectra recorded by OSA as the temperature changed from 35 °C to 95 °C is shown in Fig. 7(a), where obvious red shifts can be observed. Since the original image is very dense and has a high degree of coincidence, the lower envelopes of the data are used to evaluate the sensor's performance in the subsequent analysis. The lower envelop data obtained by OriginPro 2022 beta2 are shown in Fig. 7(b), where obvious red shifts can be observed with the temperature increase in the range of 1530∼1605 nm. The lower envelops, involving two distinct dips (Dip 1 and Dip 2) were selected and the dip near 1560 nm was affected by the transmission spectrum of the HC-ARF. The dips have different shifts and apply to
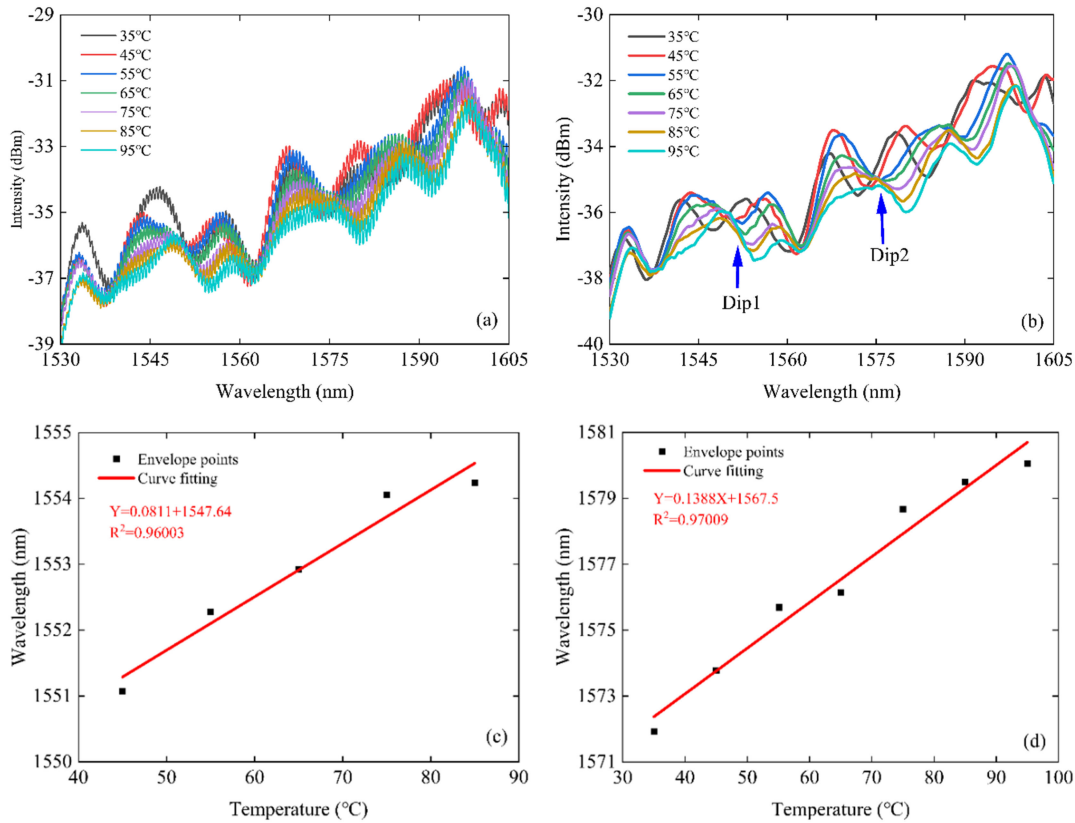
Fig. 7. (a) the measured spectra at the temperature variation range of 35 °C∼95 °C, (b) the lower envelopes of the measuring spectra using a 20 mm-SMF2, (c) the linear fitting of Dip 1 at the temperature variation range of 45 °C∼85 °C, (d) the linear fitting of Dip2 at the temperature variation range of 35 °C∼95 °C.

different temperature ranges. The linear fitting of the wavelength variation of Dip 1 with temperature change from 45 °C to 85 °C at the range of 1550 nm∼1555 nm is shown in Fig. 7(c), and the corresponding function is "Y = 0.0811X+1547.64" (Y is wavelength in nanometer and X is temperature in degree Celsius). As a result, based on Dip1, the temperature sensitivity was 81.1 pm/°C and R-square was 0.96003. Fig. 7(d) shows the linear fitting of Dip 2 with temperature change from 35 °C to 95 °C at the range of 1571 nm∼1581 nm, and the corresponding function is "Y = 0.1388X + 1567.5". Hence, based on Dip 2, the temperature sensitivity was as high as 138.8 pm/°C and R-square was 0.97009. The disparity of the two sensitivities was mainly caused by the difference of the interference modes at different wavebands due to the change of transmission loss of the fabricated HC-ARF. We can see that a good liner relationship was obtained throughout the whole temperature range, indicating that there was an obvious interference occurrence under this length setting of the Au-coated SMF2 (20 mm).

Experiments were conducted to verify the influence of the SMF2 length on the sensor's performance. The length of the SMF2 was lengthened to 34 mm while the length of the HC-ARF was kept the same. The temperature was adjusted from 45 °C to 85 °C. The FPI spectrum measured at 55 °C is shown in Fig. 8(a), and the result after going through the Fast Fourier Transform (FFT) is shown in Fig. 8(b). As expected, the FFT curve is similar to that in Fig. 6(a). The lower envelops of

the measured spectra are shown in Fig. 8(c), together with the selected envelop range. In this experiment, the dip located from 1554 nm to 1557 nm was focused to evaluate the sensitivity. The liner fitting curve of the envelop data with the temperature is shown in Fig. 8(d) and the corresponding function is "Y = 0.0485X+1552.51", indicating a sensitivity of 48.5 pm/°C with a R-square of 0.97505. This sensitivity was only 60% of that obtained in the previous experiment at the similar waveband (∼81.1 pm/°C). This result was consistent with the theoretical analysis based on Eq. (14) and Eq. (15) which predicted an increase in the length of SMF2 would reduce the sensing sensitivity. Therefore, it was confirmed that the sensitivity of the proposed sensor can be adjusted by varying the length of SMF2. In addition, it suggested that the sensitivity had much room for enhancement, namely, with the improvement of cutting and splicing technology, a higher sensitivity (over 138.8 pm/°C) can be obtained by further shortening the length of SMF2.

When SMF2 was lengthened to 45 mm, the Vernier amplification effect was further reduced. The envelope of the magnitude spectrum is presented in Fig. 9(a). Not similar to Fig. 7 and Fig. 8, the shift of envelope was not obvious, which was ∼1550 nm at the temperature variation range of 55∼85 °C. The liner fitting curve of the envelop data from 55 °C to 85 °C is shown in Fig. 9(b) and the corresponding function is "Y = 0.013X+1549.2". The sensitivity of ∼13 pm/°C with a R-square of 0.89418 was much worse than the experimental data obtained using the 34 mm long SMF2.
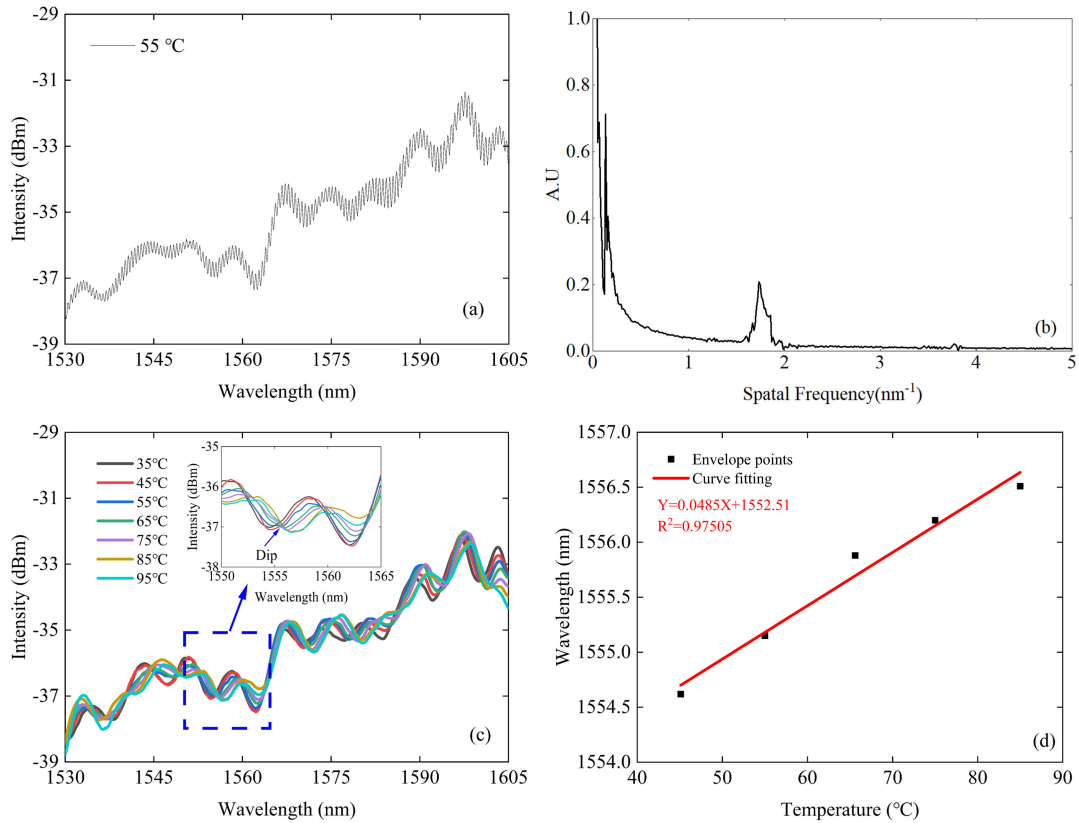
Fig. 8. (a) The FPI spectrum measured at 55 °C, (b) the corresponding FFT. (c) The lower envelopes of the measuring spectra using a 34 mm-SMF2, (d) the linear fitting at the temperature variation range of 45 °C∼85 °C.
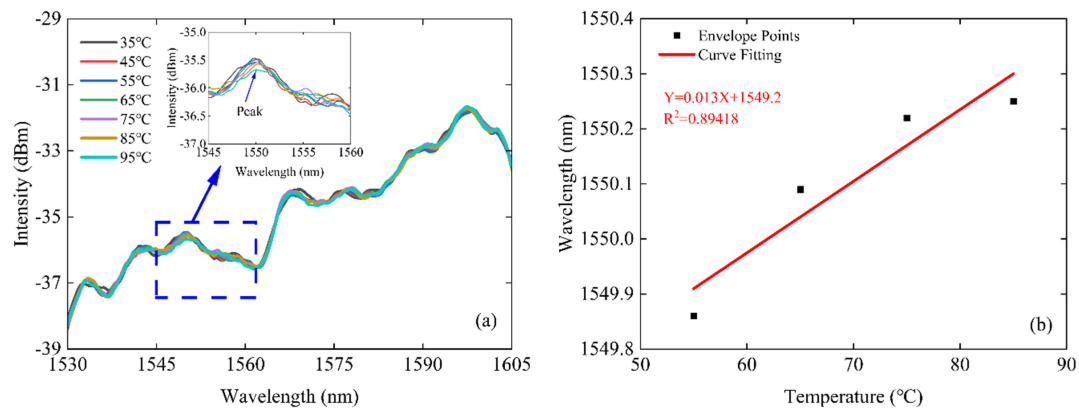

Fig. 9. (a) The lower envelopes of the measuring spectra using a 45 mm-SMF2, (b) the linear fitting at the temperature variation range of 55 °C∼85 °C.

Similar experiments were conducted with the further increase of the SMF2 length (70 mm, 81 mm, 95 mm, 115 mm and 134 mm) at the temperature variation range of 35∼95 °C, and the envelopes of the measured spectral waveform are shown in Fig. 10(a)∼(e). In these cases, the development of the envelopes became messy with the length of SMF2 increase. Moreover, the performance of the proposed sensor structure with a 170 mm long SMF2 but without the Au film was investigated (see Fig. 10(f)). In comparison, it was clear that all the spectra were extremely similar, which indicated that the sensitivity

enhancement brought by the Au film had already been offset by the lengthening of SMF2.

Table I presents a performance comparison between our proposed sensor and those reported previously [6], [8], [9], [11], [19]. Compared with these temperature sensors based on different working schemes, the sensor of this work has the advantages of good temperature sensitivity, easy manufacture, and compact structure. More importantly, the temperature sensitivity can be further improved by shortening the length of the Au-coated SMF with the advancement in cutting and splicing technology.
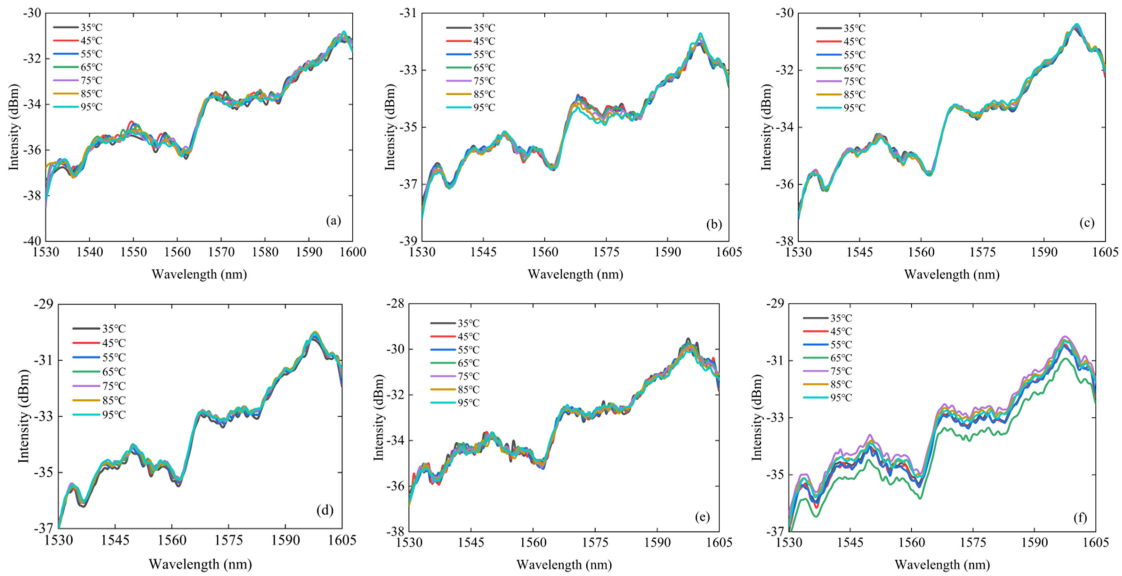
Fig. 10. The lower envelopes of the measuring spectra using (a) a 70 mm-SMF2, (b) a 81 mm-SMF2, (c) a 90 mm-SMF2, (d) a 115 mm-SMF2, (e) a 134 mm-SMF2, (f) a 170 mm-SMF2 without the Au film.

TABLE I
COMPARISON BETWEEN THE PROPOSED SENSOR AND THE PREVIOUSLY REPORTED ONES

Type	Sensitivity	Temperature range	Difficulty of the preparation	Ref
FBG	19.4 pm/°C	20°C~130°C	MID	6
SOE	1.04×10^{-3} °C^{-1}	25°C~100°C	MID	8
MI	40 pm/°C	50°C~250°C	MID	9
MZI	33.4 pm/°C	Room temperature ~1005°C	EASY	11
FPI	44 pm/°C	0~175°C	HARD	19
FPI	138.8 pm/°C	35~95°C	EASY	@ this work

V. CONCLUSION

In summury, a FPI temperature sensor was proposed based on a 2 mm self-made HC-ARF and an 20 mm Au-coated SMF. Experimental investigation found that with the temperature changing from 35 °C to 95 °C, this sensor can achieve a sensitivity of 138.8 pm/°C at the waveband of 1571 nm ~1581 nm when temperature vary from 45 °C to 85 °C and 81.1 pm/°C at the waveband of 1550 nm ~to 1555 nm when temperature vary from 45 °C to 85 °C. Theoretical analysis suggested that its sensing sensitivity can be adjusted by varying the length of the Au-coated SMF with Vernier effect, and this was confirmed by a subsequent experiment where the SMF length was varied from 20 mm to 170 mm. The design of this HC-ARF based FPI sensor offers a simple sensitivity control method and it can achieve high and diverse sensitivities at different wavebands. The sensor is easy to manufacture, compact in structure, and convenient in performance control, which can be applied for a wide range of biological and chemical applications.

REFERENCES

[1] S. Cao et al., "Highly sensitive surface plasmon resonance biosensor based on a low-index polymer optical fiber," Opt. Exp., vol. 26, no. 4, pp. 3988–3994, Feb. 2018.
[2] H. Jiao, L. Feng, N. Liu, and Z. Yang, "Improvement of long-term stability of hollow-core photonic-crystal fiber optic gyro based on single-polarization resonator," Opt. Exp., vol. 26, no. 7, pp. 8645–8655, Mar. 2018.
[3] Y. Li, F. Teng, B. Yang, Z. Zhang, Y. Zhao, and Y. Zhang, "Noise analysis of hollow core photonic crystal fiber optic gyroscope," Optik, vol. 225, Jan. 2021, Art. no. 165849.
[4] X. R. Liao, H. F. Chen, and D. N. Wang, "Ultracompact optical fiber sensor for refractive index and high-temperature measurement," J. Lightw. Technol., vol. 32, no. 14, pp. 2531–2535, Jun. 2014.
[5] Z. Zhu, D. Ba, L. Liu, L. Qiu, S. Yang, and Y. Dong, "Temperature-compensated multi-point refractive index sensing based on a cascaded Fabry-Perot cavity and FMCW interferometry," Opt. Exp., vol. 29, no. 12, pp. 19034–19048, Jun. 2021.
[6] Y. Wang et al., "Simultaneous measurement of temperature and strain based on a hollow core Bragg fiber," Opt. Lett., vol. 45, no. 22, pp. 6122–6125, Nov. 2020.
[7] G. Li, L. Ji, G. Li, J. Su, and C. Wu, "High-resolution and large-dynamic-range temperature sensor using fiber Bragg grating Fabry-Pérot cavity," Opt. Exp., vol. 29, no. 12, pp. 18523–18529, Jun. 2021.
[8] A. Leal-Junior, A. Frizera-Neto, C. Marques, and M. J. Pontes, "A polymer optical fiber temperature sensor based on material features," Sensors, vol. 18, no. 1, pp. 301–310, Jan. 2018.
[9] L. Duan et al., "Heterogeneous all-solid multicore fiber based multipath Michelson interferometer for high temperature sensing," Opt. Exp., vol. 24, no. 18, pp. 20210–20218, Aug. 2016.
[10] G. Statkiewicz-Barabach, J. Olszewski, P. Mergo, and W. Urbanczyk, "Hydrostatic pressure and temperature measurements using an in-line Mach-Zehnder interferometer based on a two-mode highly birefringent microstructured fiber," Sensors, vol. 17, no. 7, Jul. 2017, Art. no. 1648.

[11] D. Liu *et al.*, "Hollow core fiber based interferometer for high-temperature (1000 °C) measurement," *J. Lightw. Technol.*, vol. 36, no. 9, pp. 1583–1590, May 2018.

[12] Z. Li, C. Liao, Y. Yang, Y. Wang, and Y. Wang, "High-sensitivity gas pressure sensor based on a multimode interferometer using hollow-core tube lattice fiber," *Opt. Lett.*, vol. 45, no. 16, pp. 4571–4574, Aug. 2020.

[13] Z. Chen *et al.*, "High-temperature sensor based on Fabry-Perot interferometer in microfiber tip," *Sensors*, vol. 18, pp. 202–208, Jan. 2018.

[14] J. Tian, Z. Li, Y. Sun, and Y. Yao, "High-sensitivity fiber-optic strain sensor based on the Vernier effect and separated Fabry–Perot interferometers," *J. Lightw. Technol.*, vol. 37, no. 21, pp. 5609–5618, Nov. 2019.

[15] P. Urquhart, "Compound optical-fiber-based resonators," *J. Opt. Soc. Amer. A*, vol. 5, no. 6, pp. 803–812, Jun. 1988.

[16] D. Dai, "Highly sensitive digital optical sensor based on cascaded high-Q ring-resonators," *Opt. Exp.*, vol. 17, no. 26, pp. 23817–23822, Dec. 2009.

[17] M. Quan, J. Tian, and Y. Yao, "Ultra-high sensitivity Fabry–Perot interferometer gas refractive index fiber sensor based on photonic crystal fiber and Vernier effect," *Opt. Lett.*, vol. 40, no. 21, pp. 4891–4894, Oct. 2015.

[18] C. Zhu and J. Huang, "Sensitivity-enhanced microwave-photonic optical fiber interferometry based on the Vernier effect," *Opt. Exp.*, vol. 29, no. 11, pp. 16820–16832, May 2021.

[19] M. S. Ferreira, J. Bierlich, J. Kobelke, J. L. Pinto, and K. Wondraczek, "Negative curvature hollow core fiber sensor for the measurement of strain and temperature," *Opt. Exp.*, vol. 29, no. 4, pp. 5808–5818, Feb. 2021.

[20] Y. Zheng *et al.*, "Anti-resonant reflecting effect in large-core hollow-core photonic crystal fiber for temperature sensing," in *Proc. 18th Int. Conf. Opt. Commun. Netw.*, 2019, pp. 1–3, doi: 10.1109/ICOCN.2019.8934394.

[21] C. Wei, R. J. Weiblen, C. R. Menyuk, and J. Hu, "Negative curvature fibers," *Adv. Opt. Photon*, vol. 9, no. 3, pp. 504–561, Sep. 2017.

[22] F. Yu and J. C. Knight, "Negative curvature hollow-core optical fiber," *IEEE J. Sel. Topics Quantum Electron.*, vol. 22, no. 2, pp. 146–155, Mar./Apr. 2016, Art no. 4400610, doi: 10.1109/JSTQE.2015.2473140.

[23] A. Taranta *et al.*, "Exceptional polarization purity in antiresonant hollow-core optical fibres," *Nat. Photon.*, vol. 14, pp. 504–510, May 2020.

[24] Y. Zheng *et al.*, "Temperature-independent bending sensor based on hollow core microstructured optical fiber," in *Proc. IEEE Photon. Conf.*, 2019, pp. 1–2, doi: 10.1109/IPCon.2019.8908336.

[25] H. Yu, Z. Luo, Y. Zheng, J. Ma, Z. Li, and X. Jiang, "Temperature-insensitive vibration sensor with Kagomé Hollow-core fiber based Fabry–Perot interferometer," *J. Lightw. Technol.*, vol. 37, no. 10, pp. 2261–2269, 2019, doi: 10.1109/JLT.2019.2901845.

[26] C. Yao *et al.*, "Sub-ppm CO detection in a sub-meter-long hollow-core negative curvature fiber using absorption spectroscopy at 2.3 μm," *Sensors Actuators B Chem.*, vol. 303, Jan. 2020, Art. no. 127238.

[27] M. Nissen *et al.*, "UV absorption spectroscopy in Water-filled antiresonant Hollow core fibers for pharmaceutical detection," *Sensors*, vol. 18, no. 2, Feb. 2018, Art. no. 478.

[28] A. Sharma, S. Xie, R. Zeltner, and P. St. J. Russell, "On-the-fly particle metrology in hollow-core photonic crystal fibre," *Opt. Exp.*, vol. 27, no. 24, pp. 34496–34504, Nov. 2019.

[29] X. L. Liu *et al.*, "Characterization of a liquid-filled nodeless anti-resonant fiber for biochemical sensing," *Opt. Lett.*, vol. 42, no. 4, pp. 863–866, Feb. 2017.

[30] X. Huang, J. Zang, and S. Yoo, "Sensing applications of double hollow-core anti-resonant fiber based modal interferometer," in *Proc. Conf. Lasers Electro-Opt.*, 2018, pp. 1–2.

[31] P. Chen and X. Shu, "Refractive-index-modified-dot Fabry-Perot fiber probe fabricated by femtosecond laser for high-temperature sensing," *Opt. Exp.*, vol. 26, no. 5, pp. 5292–5299, Feb. 2018.

[32] G. Zhang *et al.*, "High temperature Vernier probe utilizing photonic crystal fiber–based Fabry-Perot interferometers," *Opt. Exp.*, vol. 27, no. 26, pp. 37308–37317, Dec. 2019.

[33] H. Cheng, S. Wu, Q. Wang, S. Wang, and P. Lu, "In-line hybrid fiber sensor for curvature and temperature measurement," *IEEE Photon. J.*, vol. 11, no. 6, Dec. 2019, Art. no. 6803311, doi: 10.1109/JPHOT.2019.2944988.

[34] L. Xie, B. Sun, M. Chen, and Z. Zhang, "Sensitivity enhanced temperature sensor with serial tapered two-mode fibers based on the Vernier effect," *Opt. Exp.*, vol. 28, no. 22, pp. 32447–32455, Oct. 2020.

[35] L. Kong *et al.*, "Cylinder-type fiber-optic Vernier probe based on cascaded Fabry–Perot interferometers with a controlled FSR ratio," *Appl. Opt.*, vol. 57, no. 18, pp. 5043–5047, Jun. 2018.

[36] Y. Zhao, P. Wang, R. Lv, and X. Liu, "Highly sensitive air-flow sensor based on Fabry–Perot interferometer and Vernier effect," *J. Lightw. Technol.*, vol. 34, no. 23, pp. 5351–5356, Dec. 2016, doi: 10.1109/JLT.2016.2615054.